Criterion for vortex breakdown on shock wave and streamwise vortex interactions

Toshihiko Hiejima*

Department of Aerospace Engineering, Osaka Prefecture University, 1-1 Gakuen-cho, Nakaku, Sakai, Osaka 599-8531, Japan

(Received 19 March 2014; published 19 May 2014)

The interactions between supersonic streamwise vortices and oblique shock waves are theoretically and numerically investigated by three-dimensional (3D) Navier-Stokes equations. Based on the two inequalities, a criterion for shock-induced breakdown of the streamwise vortex is proposed. The simple breakdown condition depends on the Mach number, the swirl number, the velocity deficit, and the shock angle. According to the proposed criterion, the breakdown region expands as the Mach number increases. In numerical simulations, vortex breakdown appeared under conditions of multiple pressure increases and the helicity disappeared behind the oblique shock wave along the line of the vortex center. The numerical results are consistent with the predicted breakdown condition at Mach numbers 2.0 and 3.0. This study also found that the axial velocity deficit is important for classifying the breakdown configuration.

DOI: 10.1103/PhysRevE.89.053017 PACS number(s): 47.40.Nm, 47.32.cd

I. INTRODUCTION

The vortex breakdown phenomenon in incompressible flows has been widely investigated [1–3]. The physical effects of vortex breakdown are sudden increase of vortex core size, reversed flow and stagnation points, and highly unstable structures. The onset of breakdown is governed by the swirl strength, adverse pressure gradients, and the formation of a stagnation point near the axis. The swirl number especially affects the breakdown condition. At high Reynolds number, the breakdown configuration is categorized into two types: *bubble type* and *spiral type*.

Less is known about vortex breakdown at high speeds. However, an oblique shock wave impinging on wakes or streamwise vortices induces the breakdown beyond a critical value of the pressure rise across the shock. Thus, supersonic vortex breakdown occurs when the vortex interacts with shock waves. This phenomenon was detailed in Delery [4] and Kalkhoran and Smart [5]. The interaction between streamwise vortices and shocks depends on the swirl intensity in the vortex, the axial velocity deficit at the vortex center, and the shock strength, quantified by the Mach number. An example of where such interaction is problematic is the external flow of a high speed vehicle, where the streamwise vortex generated from the canard may cross the shock wave developing on the main wing. If sufficiently severe, this interaction can affect the aerodynamic performance of the vehicle. Another example is internal flow. Zatoloka *et al.* [6] first investigated the effect of such interactions on the inlet performance of a supersonic vehicle. This study was motivated by concern that shock wave and vortex interactions cause inlet unstart of the engine. Besides being problematic, shock wave and vortex interactions confer certain advantages, because streamwise vortices encourage supersonic mixing. Thus, they can enhance fuel-air mixing and flame holding in supersonic combustion ramjet engines. For instance, by interacting an oblique shock wave with a jet or streamwise vortices, Marble *et al.* [7] showed that the resulting baroclinic torque generates a useful vorticity field and a disrupted streamwise vortex.

Shock wave and vortex interactions have been classified into two categories: normal shock wave and vortex interaction (NSVI) and oblique shock wave and vortex interaction (OSVI). Figure 1 is a schematic of OSVI. Considering the difference in pressure gradients, NSVI more readily induces vortex breakdown than OSVI. Early experiments on vortex breakdown by NSVI [4,8,9] revealed three types of interaction: weak, moderate, and strong. In these investigations, the size of the interaction region was compared with the size of the diameter of the upstream vortex core. Kandil *et al.* [11], Meadows *et al.* [12], Metwally *et al.* [8], and Erlebacher *et al.* [13] conducted numerical studies of NSVI. Their numerical visualizations revealed the flow field within the interaction region, which is difficult to visualize experimentally. However, in practical applications, OSVI is more important than NSVI. In their investigations of OSVI experiments, Kalkhoran [5] and Smart [10] showed that supersonic vortex distortion in OSVI occurs at subsonic speeds, as shown in Fig. 2. Klaas *et al.* [14] measured the axial and tangential Mach number profiles in OSVI using laser Doppler velocimetry and particle image velocimetry. OSVI has also been numerically investigated by Corpening and Anderson [15], Rizzetta [16], Nedungadi and Lewis [17], Thomer *et al.* [18], and Zheltovodov *et al.* [19]. Several numerical works have shown that characteristic vortical structures, such as helices, are generated by the shock wave and vortex interaction. These structures strongly indicate that the breakdown configuration relies on upstream conditions (the freestream Mach number, circulation, and axial velocity deficit). The axial velocity deficit in the upstream vortex (depicted in Fig. 3) plays an important causative role in vortex breakdown [16–18], and is also held responsible for discrepancies between numerical simulations and experiments. Despite these considerations, the unstable properties of upstream streamwise vortices have been treated as less important than the interaction region.

Several researchers [20–22] have attempted to predict shock-induced breakdown. In upstream vortex models with no velocity deficit, the critical swirl number of NSVI breakdown was shown to decrease with increasing Mach number. However, theoretical studies of OSVI have yet to be validated by experiments and numerical simulations. As described later,

*hiejima@aero.osakafu-u.ac.jp

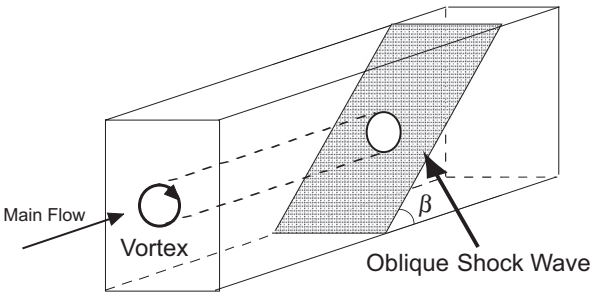

FIG. 1. Schematic of an oblique shock wave interacting with a vortex at shock angle β.

the velocity deficit of upstream vortices has been rarely considered. Aimed at predicting supersonic vortex breakdown as accurately as possible, this study proposes a mathematical formulation of the onset of oblique shock-induced vortex breakdown in streamwise vortices with an axial velocity deficit.

This paper theoretically describes the interaction between supersonic streamwise vortices and shock waves. Section II defines the basic flow of the upstream vortices. A criterion for shock-induced vortex breakdown is proposed in Sec. III. Section IV derives a numerical formulation of the Navier-Stokes equations. The proposed theory of supersonic vortex breakdown is verified in Sec. V. This section demonstrates how the breakdown is determined from the numerically evaluated static pressure and helicity density. It also considers the effects of the circulation and Mach number on breakdown. Conclusions are presented in Sec. VI.

II. UPSTREAM STREAMWISE VORTICES

The upstream streamwise vortices are assumed to be steady and axisymmetric. The three velocity components, density, pressure, temperature, and entropy are expressed in cylindrical polar coordinates (r,θ,x) as $u_r,u_\theta,u_x,\rho,p,T$, and S, respectively. Supersonic velocities are known to be well fitted by the velocity profiles of the Batchelor vortex

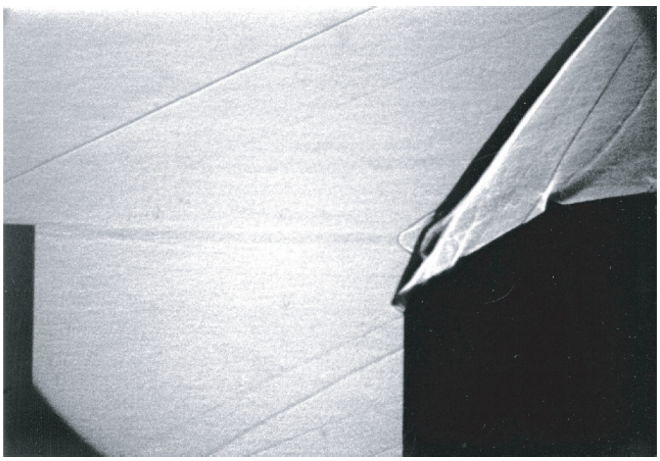

FIG. 2. Shadow graphs of the flow during the interaction of a strong vortex with an oblique shock at $M_\infty = 2.49$, by Smart *et al.* [10], reproduced with permission. Copyright 1998 Springer.

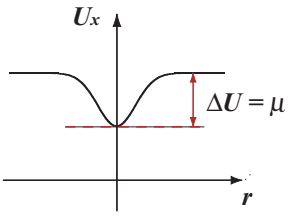

FIG. 3. (Color online) Conceptual diagram of an axial velocity profile and the velocity deficit.

[4,5,8,9]. Thus, the axial vorticity ω_x^* and the axial velocity u_x^* are represented by Eqs. (1) and (2), respectively. (Hereafter, dimensional quantities are superscripted.)

$$\omega_x^*(r^*) = \omega_{\max}^* e^{-Cr^{*2}}, \tag{1}$$

$$u_x^*(r^*) = U_\infty^* - \Delta U_x^* \, e^{-D r^{*2}}, \tag{2}$$

where $\omega_{\max}^*$ denotes the maximum axial vorticity, U_∞^* is the freestream velocity, and ΔU_x^* is the axial velocity deficit. C and D are constant for the profiles. The vortex radius is quantified by the swirl scale δ_s^* given by

$$\delta_s^* = \sqrt{\frac{\Gamma^*}{\pi\, \omega_{\max}^*}} = \frac{1}{\sqrt{C}}, \tag{3}$$

where Γ^* represents the total circulation of the whole distributed axial vorticity. Equation (2) gives rise to an azimuthal vorticity field. The thickness of the azimuthal vorticity $\delta_{\omega_\theta}^*$ is defined as

$$\delta_{\omega_\theta}^* = \frac{u_x^*(\infty) - u_x^*(0)}{\left.\frac{\partial u_x^*}{\partial r}\right|_{\max}} = \sqrt{\frac{e}{2D}} = \frac{1.165\ldots}{\sqrt{D}}. \tag{4}$$

Since the azimuthal vorticity thickness and the swirl scale are defined on similar scales, we assume that $C = D$.

The swirl parameter S_w, which characterizes the vortex strength, is equivalent to nondimensional circulation of a streamwise vortex:

$$S_w = \frac{\Gamma^*}{U_\infty^*\, \delta_s^*} \simeq \frac{1}{Ro}, \tag{5}$$

which is equivalent to the inverse of a Rossby number Ro. The swirl ratio τ and the helix angle Θ are defined as

$$\tau = \frac{u_{\theta,\max}^*}{U_\infty^*}, \quad \Theta = \tan^{-1}\tau. \tag{6}$$

Here the freestream Mach number M_∞ and Reynolds number Re are given by

$$M_\infty = \frac{U_\infty^*}{\sqrt{\gamma\, R^*\, T_\infty^*}}, \quad Re = \frac{\rho_\infty^*\, U_\infty^*\, \delta_s^*}{\eta_\infty^*}, \tag{7}$$

where T_∞^* is the freestream temperature, R^* is the gas constant, γ is the ratio of specific heats, and η_∞^* is the viscosity.

The reference length of a streamwise vortex is defined as δ_s^*. Using the freestream sonic velocity $c_\infty^*(=\sqrt{\gamma\, R^*\, T_\infty^*})$ and the density ρ_∞^*, the physical variables are

normalized as

$$\rho = \frac{\rho^*}{\rho^*_\infty}, \quad u_r = \frac{u^*_r}{c^*_\infty}, \quad u_\theta = \frac{u^*_\theta}{c^*_\infty}, \quad u_x = \frac{u^*_x}{c^*_\infty},$$
$$p = \frac{p^*}{\rho^*_\infty c^{*2}_\infty}, \quad T = \frac{T^*}{\gamma\, T^*_\infty}, \quad S = \frac{S^*}{C^*_v}, \tag{8}$$
$$r = \frac{r^*}{\delta^*_s}, \quad x = \frac{x^*}{\delta^*_s}, \quad t = \frac{c^*_\infty}{\delta^*_s}\, t^*,$$

where C^*_v represents the specific heat at constant volume.

The Oseen-type azimuthal velocity u_θ, obtained by integrating the axial vorticity, and the axial velocity u_x are derived from Eqs. (1) and (2), respectively:

$$r_\theta(r) = \frac{\Gamma}{2\pi r}\left(1 - e^{-r^2}\right), \quad \Gamma = 2\pi q M_\infty,$$
$$u_x(r) = M_\infty\left(1 - \mu\, e^{-r^2}\right), \tag{9}$$

where

$$q = \frac{\Gamma^*}{2\pi\, U^*_\infty\, \delta^*_s}, \quad \mu = \frac{\Delta\, U^*_x}{U^*_\infty}, \tag{10}$$

Here q and μ, respectively, denote the circulation and the velocity deficit, two important parameters of the streamwise vortices [23]. Since $S_w = 2\pi q$, this paper adopts q as the swirl parameter. It should also be noted that the velocity profiles of the upstream vortex play a role in vortex breakdown. Here we assume Batchelor vortices Eq. (9), which are destabilized by axial velocity deficits (such as wakes) to an extent that depends on their circulation with monotonically increasing [24]. By contrast, Erlebacher *et al.* [13] and Thomer *et al.* [18] used a Taylor vortex Eq. (11) as the upstream vortex:

$$u_\theta(r) = \frac{\Gamma}{2\pi} r e^{\frac{1}{2}(1-r^2)}. \tag{11}$$

This profile becomes destabilized with no axial velocity deficit, because its total circulation is zero. Since Eqs. (9) and (11) differ in their centrifugal instability, the instability of streamwise vortices should be considered in the analysis.

Breakdown onset does not appreciably depend on viscosity at high Reynolds numbers, so the basic flow can reasonably be regarded as an inviscid supersonic flow at $Re > 10^4$. For inviscid steady flows, suppose $u_r = 0$, the density $\rho(r)$ and pressure $p(r)$ in the basic flow are determined from the following equations, which depend only on r:

$$\frac{dp}{dr} = \rho\frac{u^2_\theta}{r},$$
$$\frac{dS}{dr} = \frac{1}{p}\frac{dp}{dr} - \gamma\frac{1}{\rho}\frac{d\rho}{dr}\left(S = S_\infty + \log\frac{p}{\rho^\gamma}\right). \tag{12}$$

Experiments have indicated that the total temperature is approximately uniform [4,9], while theoretical studies of compressible streamwise vortices have frequently assumed an isentropic vortex. The present study assumes spatially uniform entropies. This assumption is beneficial for investigating the effect of baroclinic torques on the vorticity generation in the interaction region.

III. CRITERIA OF SHOCK WAVE AND VORTEX INTERACTIONS

In incompressible flows, the onset of vortex breakdown can be theoretically determined in several ways [4]. Breakdown is due to strong adverse pressure gradients, and depends on the swirl parameter. As is well known, the critical swirl parameter is around $S_{w,c} \simeq 1.4$ ($Ro_c \simeq 0.707$, $\tau_c \simeq 1.2$, and $\Theta_c \simeq 50^\circ$). On the other hand, theoretical studies of shock-induced breakdown were conducted by Cattafesta [20], Mahesh [21], and Smart *et al.* [22]. Cattafesta [20] indicated that breakdown onset occurs at a swirl ratio of τ_2/τ_1 across the normal shock. The predicted dependence of breakdown limit on M_∞ has been compared with experimental results. Mahesh [21] developed a simple theory for determining the critical swirl ratios of breakdown onset at $M_\infty = 1$–5. This theory compares the momentum flux on axis to the pressure behind the shock. The assumed upstream vortex is the Rankine vortex. The predictions of the theory are consistent with numerical results [13] of NSVI when a constant axial velocity is assumed. Smart and Kalkhoran [22] perceived analogies between NSVI and boundary layer separation, and constructed a physical model based on this analogy. However, with the exception of Mahesh [21], previous theoretical analyses have assumed uniform axial velocity profiles of upstream vortices on NSVI. Also, Mahesh's theory has not been verified with regard to the axial velocity deficit yet [21]. The discrepancies between experimental results and theoretical analyses are likely to be caused by the axial velocity deficit [5,13,20]. In this respect, the abovementioned theories are inadequate. It should be noted that both the axial velocity deficit μ and the swirl parameter q contribute to the vortex instability which affects the breakdown pattern.

Here a new condition for shock-induced breakdown of the streamwise vortex is proposed, based on the pressure differences between the axis and infinite radius. A Rankine-Hugoniot relationship is used across the shock. Figure 4 shows how the upstream and downstream velocities of the shock wave interact with those of the streamwise vortex. Suppose that breakdown occurs if the net pressure difference exceeds the kinetic energy downstream of the shock wave. The onset condition of the vortex breakdown is demonstrated as follows:

$$\Delta P > \tfrac{1}{2}\rho_{2,\infty} U^2_{2,\infty}, \tag{13}$$

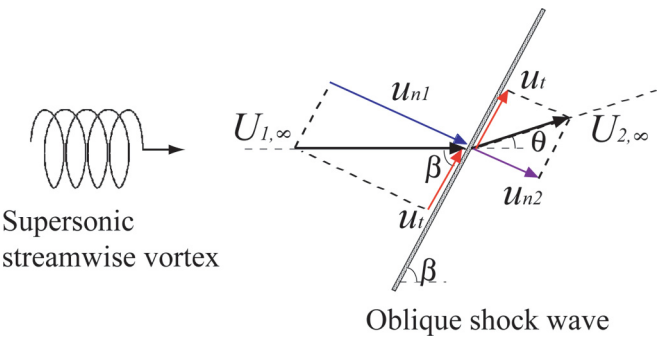

FIG. 4. (Color online) An upstream streamwise vortex and the velocity components during interaction with an oblique shock wave.

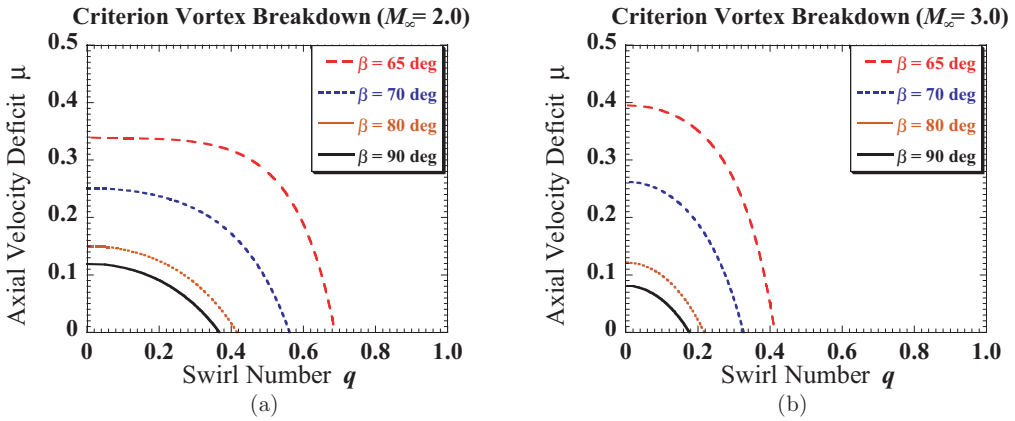

FIG. 5. (Color online) Theoretical critical curves of the interaction between streamwise vortices and oblique shock waves for various shock angles β; the interiors of curves (including the origin) indicate *stable or no effect* regions; exterior regions indicate unstable *break* regions: (a) $M_\infty = 2.0$, (b) $M_\infty = 3.0$.

where

$$\begin{aligned} \Delta P &= \Delta P_2 - \Delta P_1, \\ \Delta P_2 &= p_{2,\infty} - p_{2,c}, \\ \Delta P_1 &= p_{1,\infty} - p_{1,c}. \end{aligned} \tag{14}$$

The static pressures behind the shock $p_{2,\infty}$ and $p_{2,c}$ are, respectively, given by the Rankine-Hugoniot relation as

$$\frac{p_{2,\infty}}{p_{1,\infty}} = 1 + \frac{2\gamma}{\gamma+1}\left(M_{1,\infty}^2 \sin^2\beta - 1\right), \tag{15}$$

$$\frac{p_{2,c}}{p_{1,c}} = 1 + \frac{2\gamma}{\gamma+1}\left(M_{1,c}^2 \sin^2\beta - 1\right). \tag{16}$$

The pressure at the vortex center is derived from Eq. (12):

$$\begin{aligned} \frac{p_{1,c}}{p_{1,\infty}} &= [1-(\gamma-1)I_s(\infty)]^{\frac{\gamma}{\gamma-1}}, \\ I_s(r) &= \int_0^r \frac{u_\theta^2}{\zeta}\left[\frac{e^{-(S-S_\infty)}}{\gamma}\right]^{\frac{1}{\gamma}} d\zeta, \end{aligned} \tag{17}$$

where the subscripts 1, 2, c, and ∞ denote upstream of the shock, downstream of the shock, vortex center, and radial point at infinity, respectively.

The criterion (13) depends solely on the upstream vortex conditions $M_{1,\infty}, q, \mu$ and the shock angle $\beta(\theta)$ (where θ is the turning angle). Figure 5 shows the critical breakdown onset curves on a plot of swirl number q versus velocity deficit μ at shock angles ($\beta = 65^\circ$, 70°, 80°, and 90°) and $M_\infty = 2.0$ and 3.0. The present study is consistent with the literature [13,21] for zero the velocity deficit μ. In the region inside the curve, which contains the origin, the interactions do not affect the streamwise vortices. In the region outside the curve, the vortices interact with the shock and disintegrate. The safe region (region of no breakdown) expands with reducing shock angle β. For $q = 0$, i.e., in the presence of wake flows, when the velocity deficit is high, a burst phenomenon occurs on the shear layer. Moreover, the breakdown region expands with increasing Mach number. This result has important implications for supersonic mixing, which is constricted by compressibility effects. Furthermore, shock wave and vortex interactions do not induce streamwise vortex breakdown at $M_\infty = 2$–3 and $\beta < 60^\circ$, consistent with a large number of supersonic experiments.

Figure 6 compares the proposed theory without the velocity deficit with experimental data [20] included in the Delery breakdown limit curve. The open and closed symbols indicate the weak (no breakdown) and strong (breakdown) measured interactions, respectively. The Cattafesta criterion [20] is also plotted for comparison. The present theory accurately predicts the experimental strong interaction, but inadequately models the weak interaction. Note that the velocity deficit of vortices has not been reported in experimental studies.

IV. NUMERICAL FORMULATIONS

A. Governing equations

The governing equations are the three-dimensional, unsteady, compressible Navier-Stokes equations in general coordinates ξ_i (i = 1–3), given by

$$\frac{\partial}{\partial t}\left(\frac{\boldsymbol{Q}}{J}\right) + \frac{\partial \boldsymbol{F}_i}{\partial \xi_i} = \frac{\partial \boldsymbol{F}_{v\,i}}{\partial \xi_i}, \tag{18}$$

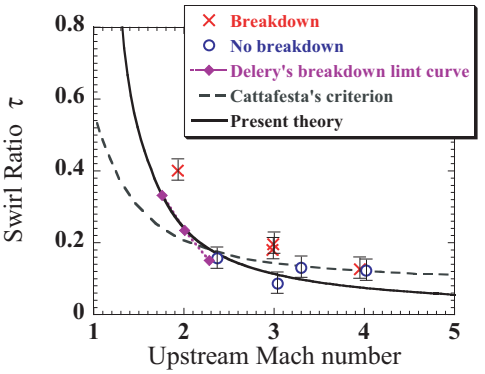

FIG. 6. (Color online) Comparison of theoretical critical curves and experimental results [20] of vortex breakdown phenomena (swirl ratio versus upstream Mach number) during vortex interaction with a normal shock wave.

$$\boldsymbol{Q} = \begin{bmatrix} \rho \\ \rho u_1 \\ \rho u_2 \\ \rho u_3 \\ e \end{bmatrix}, \quad \boldsymbol{F}_i = \begin{bmatrix} \rho\, U_i \\ \rho\, u_1\, U_i + p\,(J^{-1}\partial\xi_i/\partial x_1) \\ \rho\, u_2\, U_i + p\,(J^{-1}\partial\xi_i/\partial x_2) \\ \rho\, u_3\, U_i + p\,(J^{-1}\partial\xi_i/\partial x_3) \\ (e+p)\, U_i \end{bmatrix},$$

$$\boldsymbol{F}_{v\,i} = \begin{bmatrix} 0 \\ \tau_{1k}\,(J^{-1}\partial\xi_i/\partial x_k) \\ \tau_{2k}\,(J^{-1}\partial\xi_i/\partial x_k) \\ \tau_{3k}\,(J^{-1}\partial\xi_i/\partial x_k) \\ \beta_k\,(J^{-1}\partial\xi_i/\partial x_k) \end{bmatrix}, \quad U_i = \left(J^{-1}\frac{\partial\xi_i}{\partial x_k}\right) u_k,$$

$$\begin{aligned} J^{-1} = {} & \frac{\partial x_1}{\partial\xi_1}\left(\frac{\partial x_2}{\partial\xi_2}\frac{\partial x_3}{\partial\xi_3} - \frac{\partial x_2}{\partial\xi_3}\frac{\partial x_3}{\partial\xi_2}\right) \\ & + \frac{\partial x_1}{\partial\xi_2}\left(\frac{\partial x_2}{\partial\xi_3}\frac{\partial x_3}{\partial\xi_1} - \frac{\partial x_2}{\partial\xi_1}\frac{\partial x_3}{\partial\xi_3}\right) \\ & + \frac{\partial x_1}{\partial\xi_3}\left(\frac{\partial x_2}{\partial\xi_1}\frac{\partial x_3}{\partial\xi_2} - \frac{\partial x_2}{\partial\xi_2}\frac{\partial x_3}{\partial\xi_1}\right), \end{aligned} \tag{19}$$

where $\boldsymbol{Q}$ is a vector of conservative variables, and $\boldsymbol{F}_i$ and $\boldsymbol{F}_{v\,i}$ contain the convective and viscous fluxes, respectively. u_i are the velocity components in Cartesian coordinates. e is the total energy, and U_i denotes the velocity components on the cell interface. The Jacobian J transforms the coordinate system from physical space to computational space. $J^{-1}\partial\xi_i/\partial x_k$ are the derivatives of the coordinate conversion (i.e., the metrics):

$$\begin{aligned} & p = \rho\, T, \quad e = \frac{p}{\gamma-1} + \frac{1}{2}\rho\, u_k\, u_k, \\ & \tau_{ij} = \frac{\eta(T)}{Re_M}\left(\frac{\partial u_i}{\partial x_j} + \frac{\partial u_j}{\partial x_i} - \frac{2}{3}\delta_{ij}\frac{\partial u_k}{\partial x_k}\right), \\ & q_i = -\frac{\gamma}{(\gamma-1)}\frac{\eta(T)}{Re_M\, Pr}\frac{\partial T}{\partial x_i}, \quad \beta_i = u_i\,\tau_{ij} + q_i, \end{aligned} \tag{20}$$

where τ_{ij} is the viscous stress tensor, and q_i is the conductive heat flux. The Reynolds number, which is based on the sonic velocity, is defined as $Re_M = (\rho^*_\infty\, c^*_\infty\, \delta^*_s)/\eta^*_\infty = 3.5\times 10^4$, and the Prandtl number $Pr = 0.72$. The viscosity $\eta(T)$ is calculated from Sutherland's law as follows:

$$\eta(T) = T^{3/2}\frac{1+s'}{T+s'}, \tag{21}$$

where s' depends on the freestream Mach number; $s' = 0.49$ and 0.762 for $M_\infty = 2.0$ and 3.0, respectively.

B. Numerical methods and computing conditions

The convective flux terms are discretized using the numerical flux $\boldsymbol{F}_{i,\,m+\frac{1}{2}}$ and the primitive variables vector $\boldsymbol{q}$ as follows:

$$\frac{\partial \boldsymbol{F}_i}{\partial\xi_i} \equiv \frac{\boldsymbol{F}_{i,\,m+\frac{1}{2}}(\boldsymbol{q}) - \boldsymbol{F}_{i,\,m-\frac{1}{2}}(\boldsymbol{q})}{\Delta\xi_i}, \quad \boldsymbol{q} = \begin{bmatrix} \rho \\ u_1 \\ u_2 \\ u_3 \\ p \end{bmatrix}. \tag{22}$$

The numerical flux in Eq. (22) is evaluated by an AUSMDV scheme [25]. This adapted AUSM approach is simpler and yields more accurate results than the popular Roe scheme [26]. Since the vortex and shock wave must be simulated with sufficient accuracy in the present study, high spatial accuracy of the primitive variables $\boldsymbol{q}$ is maintained by weighted interpolation at cell interfaces. This approach, developed by Deng and Zhang [27] and based on adaptive stencil interpolation, is combined with the AUSMDV scheme. The interpolated values are fifth-order accurate in the smooth regions and large gradients, such as occur in shock waves, and do not affect the spatial precision. The nonoscillation scheme operates satisfactorily without any parameter, whereas limiter functions cannot distinguish between the discontinuity front of a shock and the turning value in the azimuthal velocity profile. Moreover, the viscous flux terms are calculated by difference equations accurate to fourth order. Temporal integration adopts a four-step, fourth-order accurate scheme [28]. Direct numerical simulations are conducted for excluding the effect of turbulence models from the static pressure of the vortex center and the velocity deficit, which is deemed important in this study.

TABLE I. Computational domain and grid points.

Style (shock)	Domain size (L_X, L_Y, L_Z)	Grid points $(N_x \times N_y \times N_z)$	Vortex of axis (L_X, L_Y, L_Z)
NSVI	(80, 40, 40)	$161 \times 201 \times 201$	(0, 20, 20)
OSVI	(80, 92, 40)	$161 \times 201 \times 163$	(0, 32, 20)

The computational domain is a rectangular box with flows in the x direction. The size, grid points, and position of the inflow vortex center are presented in Table I. The grid is clustered to resolve the interaction between a streamwise vortex and a shock wave. The grid spacing is uniform inside the inner three core diameters. (The maximum azimuthal velocity occurs close to the vortex core radius.) Outside this region, the grid splays out at irregular intervals. First, a vortexless flow field is established for a given freestream Mach number and shock angle. The normal shock wave is given by the Rankine-Hugoniot relationship before and beyond $L_x = 40$. The oblique shock wave (projected at shock angle β) is subjected to the boundary conditions at the bottom of the domain, $L_X = 30, L_Y = 0$. Next the inflow is fixed with the streamwise vortex described in Sec. II. The outflow condition is extrapolated to zeroth order, since OSVI is supersonic at the boundary. In contrast, a nonreflecting boundary condition [29] is imposed for NSVI being subsonic behind the shock. A symmetric boundary condition is applied to the other boundary surface.

To verify the theoretical criteria proposed in Sec. III, the streamwise vortices are numerically interacted with shock waves at various swirl numbers q and axial velocity deficits μ of the vortices. The freestream Mach numbers are set to $M_\infty = 2.0$ and 3.0, with shock angles $\beta = 65^\circ$ and 90°.

V. RESULTS AND DISCUSSION

A. Normal shock wave and vortex interactions

First, the present theory is compared to the numerical results and previously proposed theories of NSVI. Figure 7

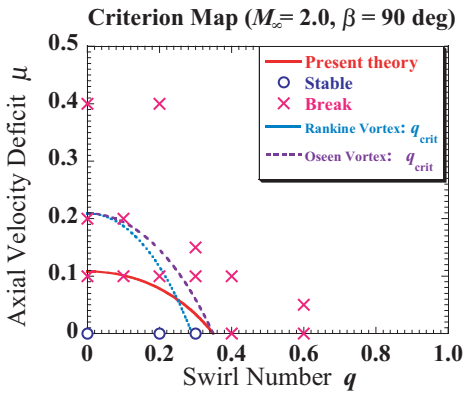

FIG. 7. (Color online) Comparison of theoretical critical curves and numerical results of vortex breakdown phenomena. The normal shock wave intercepts at $\beta = 90^\circ$ at $M_\infty = 2.0$: stable or no effect (◯); vortex breakage (×); Mahesh's theory [21] (dotted line); modified vortex model (dashed line); present theory (solid line).

shows a critical map at breakdown. The predictions of the proposed theory, Mahesh's theory [21] assuming the Rankine vortex, the modified vortex model, and the results of numerical simulations at $M_\infty = 2.0$ are plotted in this figure. The modified vortex model applies Mahesh's theory to the Oseen vortex. The method that determines whether the numerically simulated vortex remains stable or breaks up will be described in Sec. V C. The upstream vortex profile at the breakdown is influenced by the type of vortex (Rankine or Oseen). The modified vortex model successfully predicts breakdown onset at uniform axial velocity, but fails in the case of axial velocity deficit. In contrast, the proposed formulation (13) accurately predicts breakdown onset in this scenario.

Figure 8 plots the helicity density contours and the cross-sectional density contour lines (at $Z = 20$) in the wake of various streamwise vortices at $M_\infty = 2.0$. The helicity density h is

$$h = \boldsymbol{u} \cdot \boldsymbol{\omega} = u_i\, \omega_i, \tag{23}$$

where $\boldsymbol{u}$ and $\boldsymbol{\omega}$ denote the velocity and vorticity vectors, respectively. Based on previous works [4], Figs. 8(a) and 8(c) are typical of strong interactions while Fig. 8(b) exemplifies a weak interaction. Figure 8(a) is a typical bubble-type breakdown characterized by steady, symmetrically reversed flow. Shock-induced breakdown occurs in the wake [30,31] corresponding to circulation $q = 0$ on the strong adverse pressure gradient. The shock front in the interaction zone is cone shaped. Figure 8(c) displays a typical unsteady spiral-type breakdown with an asymmetric vortical structure within the entropy-shear layer [32]. The shock front structure differs from that in Figs. 8(a) and 8(b). Therefore, the character of the interaction appears to depend on whether q or μ dominates the interaction. The breakdown of vortices with a large wake profile and high circulation has previously not been distinguished from the strong interaction. In fact, all vortices exceeding a certain velocity deficit exhibit cone-bubble breakdown mode, regardless of the circulation q. Thus, it is believed that a conical symmetric bubble-type breakdown occurs if μ exerts a strong effect. Conversely, the azimuthal effect induces an asymmetric spiral-type unsteady breakdown if q is sufficiently large. The flow field properties of NSVI are summarized in Table II.

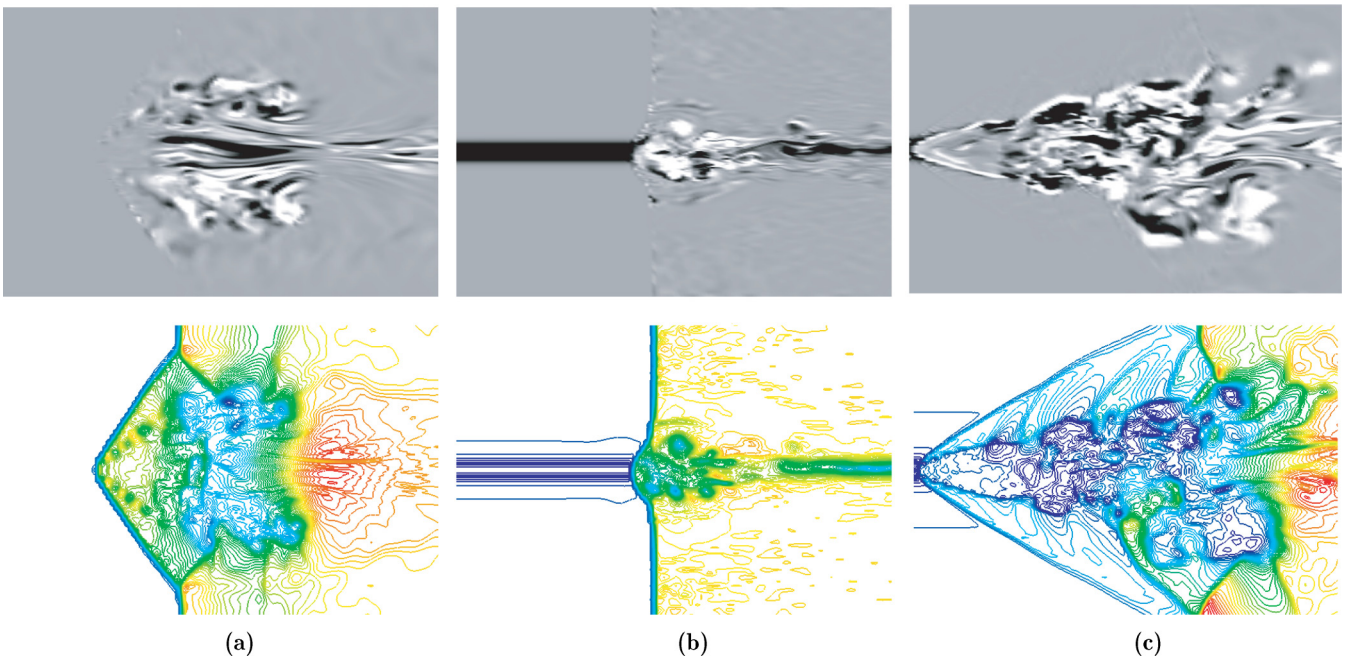

FIG. 8. (Color online) Contours of (top) helicity density, and (bottom) cross-sectional density contour lines at $Z = 20$. Vortices are intercepted by a normal shock wave at $\beta = 90^\circ$, namely NSVI: (a) $q = 0.0$, $\mu = 0.2$, (b) $q = 0.4$, $\mu = 0.0$, (c) $q = 0.6$, $\mu = 0.05$, at $M_\infty = 2.0$.

TABLE II. Vortex breakdown formations.

Type	Cone or Bubble[a]	Bubble-Spiral[b]	Spiral
Flow field	Steady Symmetry	Unsteady Asymmetry	Unsteady Asymmetry

[a]Cone shape is strong and stable with bubble-type characteristics.
[b]Combined bubble and spiral flow structures.

B. Streamwise vortex breakdown induced by oblique shock waves

Figure 9 shows the cross-sectional density contours in OSVI at $Z = 20$, including the central vortex axis, at $M_\infty = 2.0$ and 3.0. In Figs. 9(a), 9(d), and 9(e), the streamwise vortices deflecting through the oblique shock retain their vortical structures behind the shock. Contrastingly, in Figs. 9(b), 9(c), and 9(f), the shock front develops a convex structure; specifically, a bowed or blunt-nosed conical shock is formed by interactions between the vortices and the shock. The structures are clearly different, because the breakdown size grows fairly rapidly as the interaction region increases. Notably, the shock front weakens with increasing circulation and small-scale structures establish within the region. The shock position deviates in the z direction, confirming that the plane of the shock wave is slightly distorted by the swirling effect of the streamwise vortex. This effect is particularly obvious at $q > 0.4$, where it appears in the y-z plane normal to the vortex axis.

Visualization measurements [14] to date have not revealed the complete three-dimensional structure of supersonic vortex breakdown. To visualize the vortical structure of OSVI, the isosurface of the second invariant of the velocity gradient tensor [33] $\mathcal{Q}$ is plotted from a lateral viewpoint in Fig. 10. The parameters are $q = 0.2$ and 0.6, $\mu = 0.2$, and $M_\infty = 2.0$:

$$\mathcal{Q} = \frac{1}{2}(-\mathcal{S}_{ij}\mathcal{S}_{ij} + \mathcal{R}_{ij}\mathcal{R}_{ij} + \mathcal{C}^2),$$
$$\mathcal{S}_{ij} = \frac{1}{2}\left(\frac{\partial u_j}{\partial x_i} + \frac{\partial u_i}{\partial x_j}\right), \quad \mathcal{R}_{ij} = \frac{1}{2}\left(\frac{\partial u_j}{\partial x_i} - \frac{\partial u_i}{\partial x_j}\right), \quad (24)$$
$$\mathcal{C} = \frac{\partial u_k}{\partial x_k},$$

where $\mathcal{S}_{ij}$ and $\mathcal{R}_{ij}$ are the strain-rate and vorticity tensors, respectively, comprising the symmetric and asymmetric components of the velocity gradient tensor $\partial u_i/\partial x_j$, and $\mathcal{C}$ is the divergence of the velocity vectors. The left and right panels of

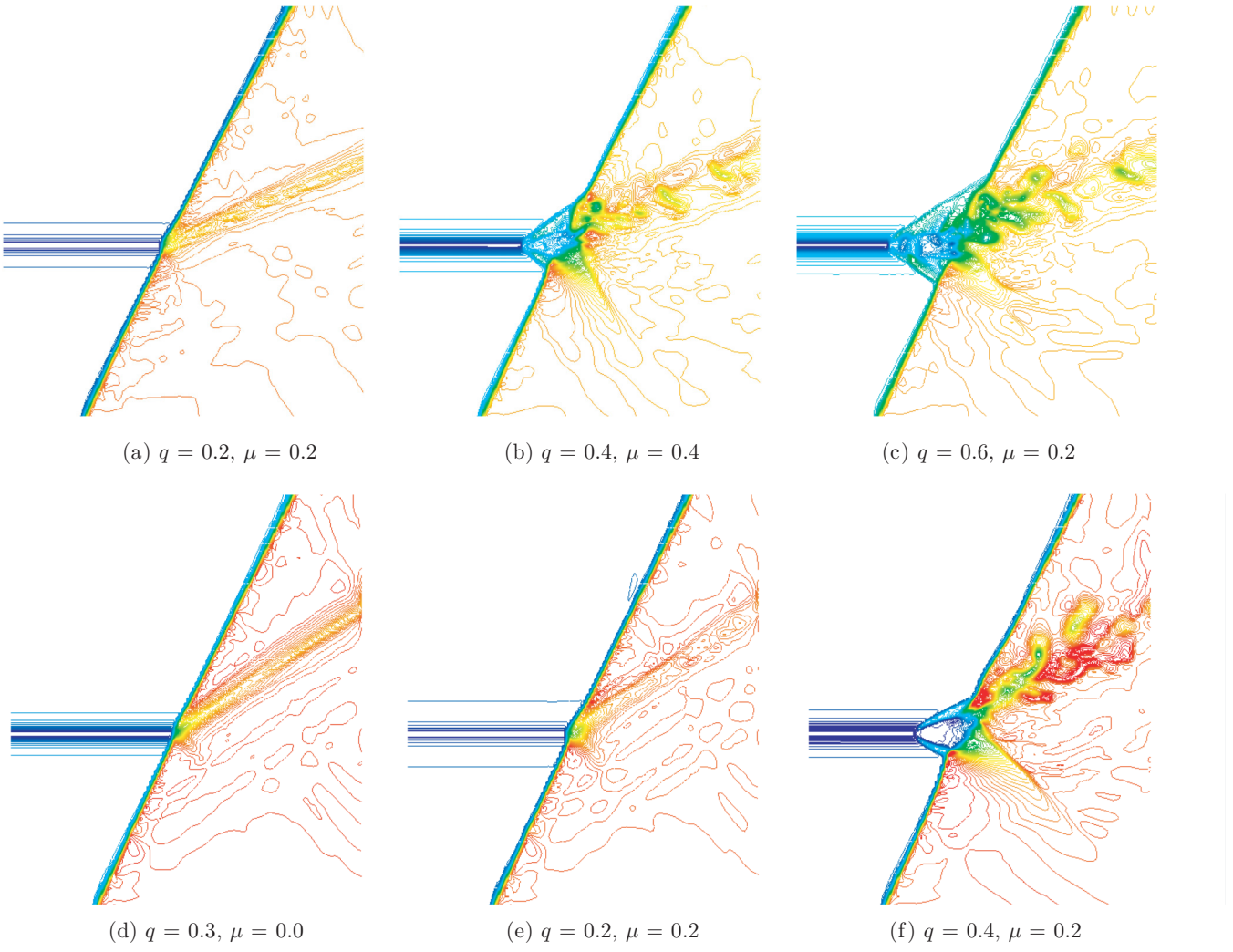

(a) $q = 0.2$, $\mu = 0.2$ (b) $q = 0.4$, $\mu = 0.4$ (c) $q = 0.6$, $\mu = 0.2$

(d) $q = 0.3$, $\mu = 0.0$ (e) $q = 0.2$, $\mu = 0.2$ (f) $q = 0.4$, $\mu = 0.2$

FIG. 9. (Color online) Cross-sectional density contour lines at $Z = 20$; (top) $M_\infty = 2.0$, (bottom) $M_\infty = 3.0$.

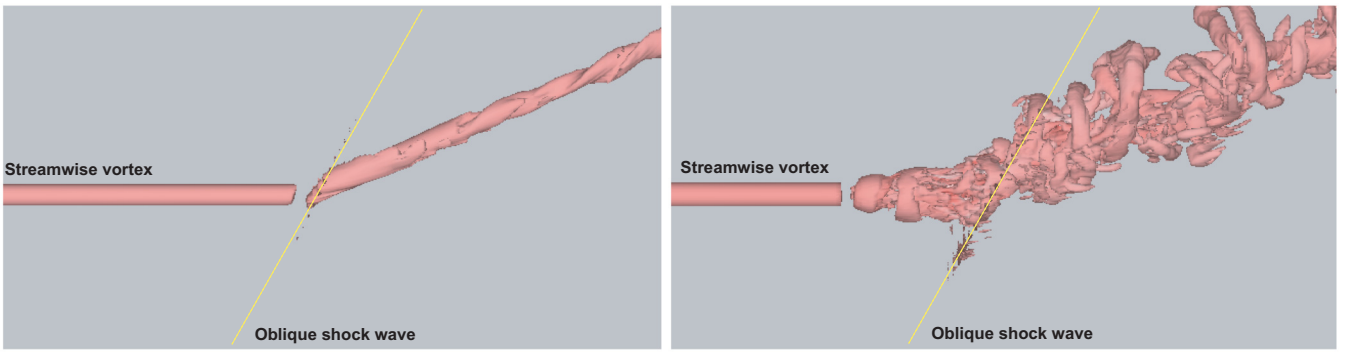

(a) (b)

FIG. 10. (Color online) Isosurface of the second invariant of the velocity gradient tensor. Side view of the interaction between a streamwise vortex and an oblique shock wave intercepting at shock angle $\beta = 65^\circ$, at $M_\infty = 2.0$; (a) $q = 0.2$, $\mu = 0.2$, (b) $q = 0.6$, $\mu = 0.2$.

Fig. 10 display a stable vortex and vortex breakdown, respectively, formed during the interaction. Indicated are the turning flows depending on the oblique shock, the effect on forward flow ahead of the shock, and the small structures formed by the vortex collapse. The vortical structures generated by the interaction deserve special mention. Thomer *et al.* [18] similarly reported that spiral vortex structures develop after the shock-induced breakdown. They investigated streamwise vortices (11) with relatively high growth rate based on linear stability at $M_\infty = 1.6$ and 2.0; $\mu = 0$ in NSVI, and $\mu = 0.1$, 0.22 in OSVI. However, the influences of large μ and small q on breakdown configurations have not been examined. Zheltovodov *et al.* [19] intended to stimulate breakdown and provided a pulsed periodic energy source at a point on the vortex axis. The results showed that spiral structures appear in the vicinity of the interference region at a small shock angle. A possible interpretation is that instability is enhanced by energy transferred to the vortex core. These results suggest that the basic instability properties of upstream vortices contribute to vortical structure formation and that streamwise vortices favor breakdown into small-scale structures. Thus, the production of spiral structures might reasonably depend on the instability characteristics.

In Fig. 10(a) the streamwise vortex is stable and robust to the shock, while breakdown occurs in Fig. 10(b). We now focus on the interference region in the breakdown scenario. Figure 11 shows the cross-sectional velocity vectors at $Z = 20$ for two swirl numbers and axial velocity deficits at $M_\infty = 2.0$. In Fig. 11(a) the region is stable in the convex shock front and its structure resembles the conical structure in NSVI. In Fig. 11(b) the region is unsteady with a spiral mode and develops a multiple-bubble structure [11]. Interestingly, the interaction regions in OSVI and NSVI are identical. Thus, the breakdown mode appears to be solely influenced by differences in the upstream vortices.

It is known from the Crocco equation that curved shock waves promote vorticity formation. Vortices generated in this way exert marked effects on breakdown. For sufficiently large Reynolds number (there is little effect of the viscosity), the inviscid vorticity equation is given by

$$\frac{D\boldsymbol{\omega}}{Dt} = (\boldsymbol{\omega}\cdot\nabla)\boldsymbol{u} - \boldsymbol{\omega}(\nabla\cdot\boldsymbol{u}) + \nabla T \times \nabla S. \qquad (25)$$

The first, second, and third terms on the right-hand side of this equation specify the stretching, dilatation, and baroclinic torque, respectively. Figure 12 shows the cross-sectional contours of the magnitude of each contributing term in Eq. (25) at $Z = 20$. The parameters are $q = 0.6$, $\mu = 0.2$, $M_\infty = 2.0$. During the interaction, the vorticity production rate is chiefly governed by the stretching term. The shock wave causes a large entropy change, as shown in Fig. 12(c). Moreover, as is well

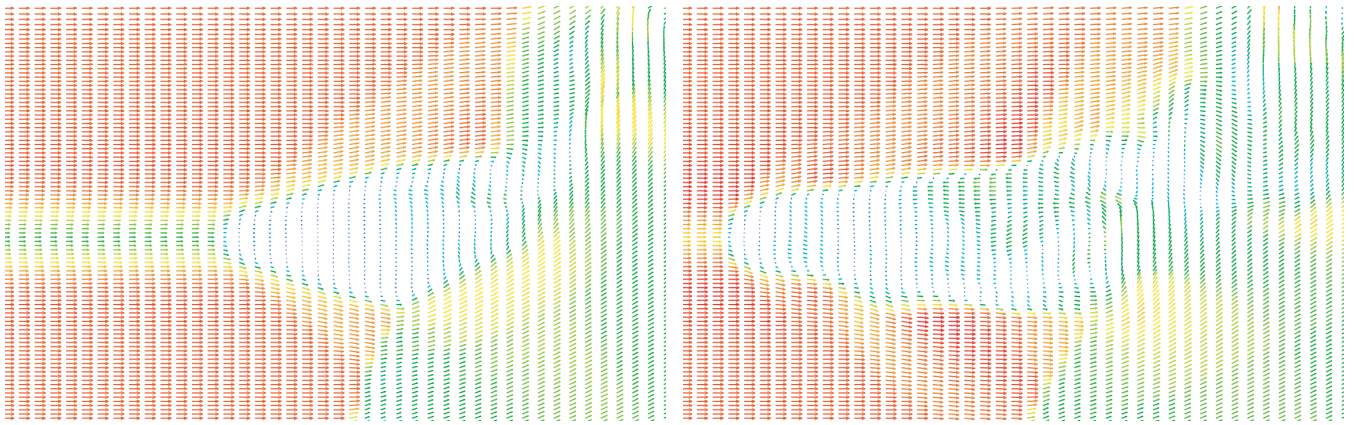

(a) (b)

FIG. 11. (Color online) Velocity vectors on the cross section at $Z = 20$, $M_\infty = 2.0$: (a) $q = 0.4$, $\mu = 0.4$, and (b) $q = 0.6$, $\mu = 0.2$.

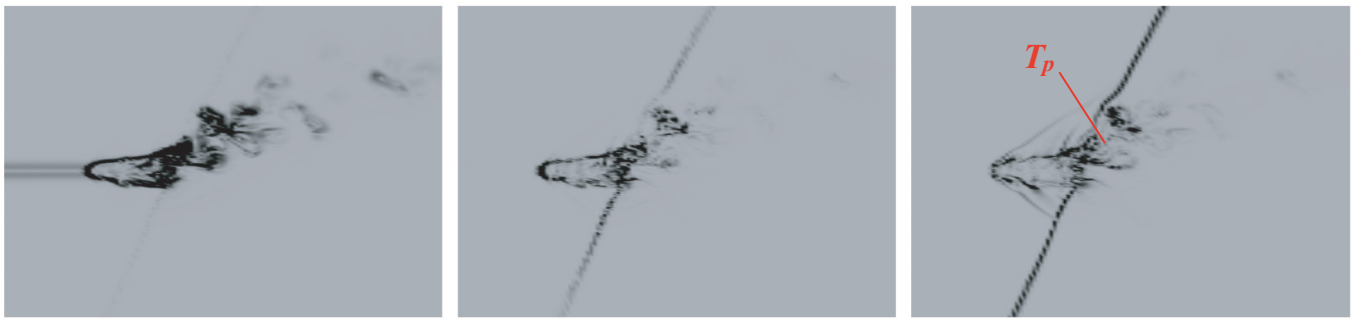

(a) (b) (c)

FIG. 12. (Color online) Cross-sectional contours of the absolute values of each term of the vorticity equation at $Z = 20$: (a) stretching term, (b) dilatation term, and (c) baroclinic torque term. Parameters: $q = 0.6$, $\mu = 0.2$, $M_\infty = 2.0$.

established, the experimentally observed entropy-shear layer [32] specifically separates the supersonic and subsonic regions within the interaction region. Furthermore, the unsteady particular vorticity is generated at the upper tag end of the entropy-shear layer within the convex shock front (point T_P in Fig. 12). The vorticity is concerned in the oscillating subsonic region.

Kalkhoran and Smart [5] experimentally demonstrated that a subsonic region is required for supersonic vortex breakdown. Although NSVI is always subsonic behind the shock, that is not necessarily so for OSVI. Therefore, in OSVI, it is important to establish the presence or absence of subsonic regions. Subsonic regions in OSVI are generated by the breakdown process. Figures 13 and 14 plot the temporal evolution of the Mach number contours for $q = 0.4$, $\mu = 0.4$ and $q = 0.6$, $\mu = 0.2$, respectively, at $M_\infty = 2.0$. Both sets of parameters yield breakdown. In these figures, the subsonic regions are marked in black color. The flow fields of $q = 0.6$, $\mu = 0.2$, being larger than those of $q = 0.4$, $\mu = 0.4$, project the interference forward. Small vortices develop behind the shock as well as inside the convex shock front. The small vortical structures grow within the interference region and are convected downstream. Although the interaction region is known to become subsonic, the profiles associated with disturbances in this region have been scarcely investigated. The local profiles in the subsonic region are plotted in Figs. 15 and 16. The axial vorticity ω_x profiles are normalized by the inflow, while those of the axial velocity u_x (the axial Mach number profiles) are normalized by the local sonic speed. Note that in the absence of breakdown, the vortex center line intersects the shock wave at $X = 45$, and the upstream vortices are certainly stable. However, the local vorticity profiles develop a striking hollowness and exhibit a strong wake with reversed axial velocity flow at $X = 39$ and $X = 34$ in Figs. 15 and 16, respectively. Thus, the altered flow fields are characterized by multiple extremal values in their vorticity profiles. Since these profiles are extremely unstable [34], small coherent structures should readily develop around the interference region between the streamwise vortex and the shock.

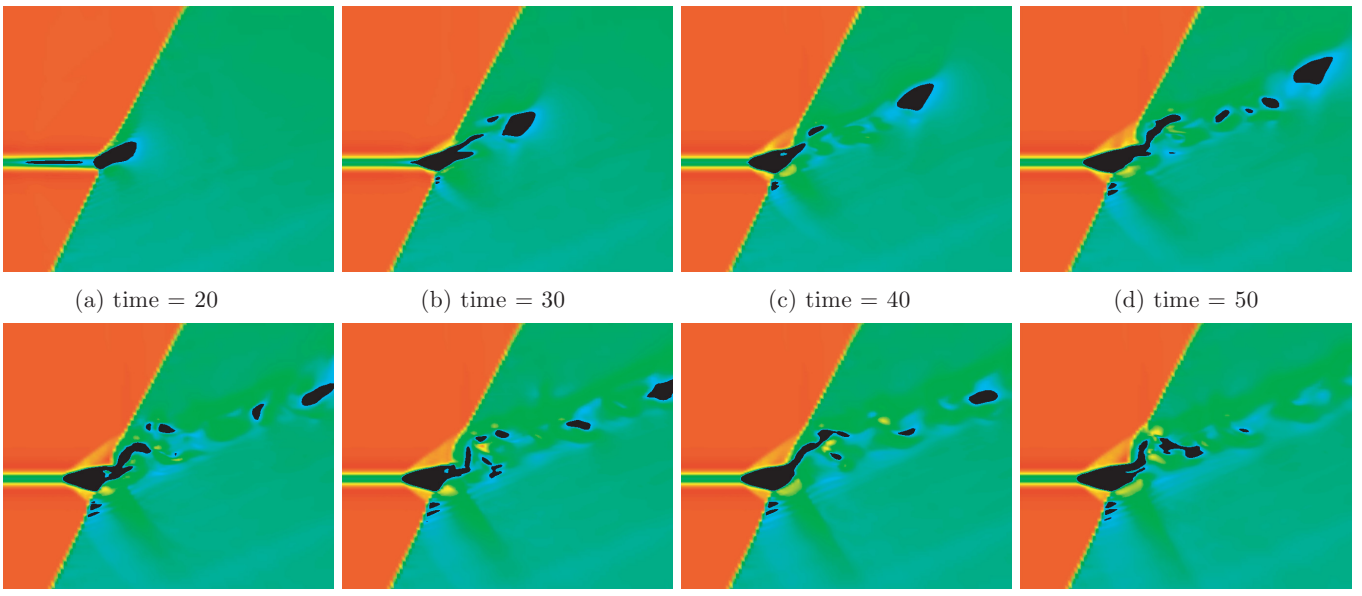

(a) time = 20 (b) time = 30 (c) time = 40 (d) time = 50

(e) time = 60 (f) time = 70 (g) time = 80 (h) time = 90

FIG. 13. (Color online) Temporal evolution of Mach number contours for $q = 0.4$, $\mu = 0.4$ at $M_\infty = 2.0$ (black areas show subsonic regions).

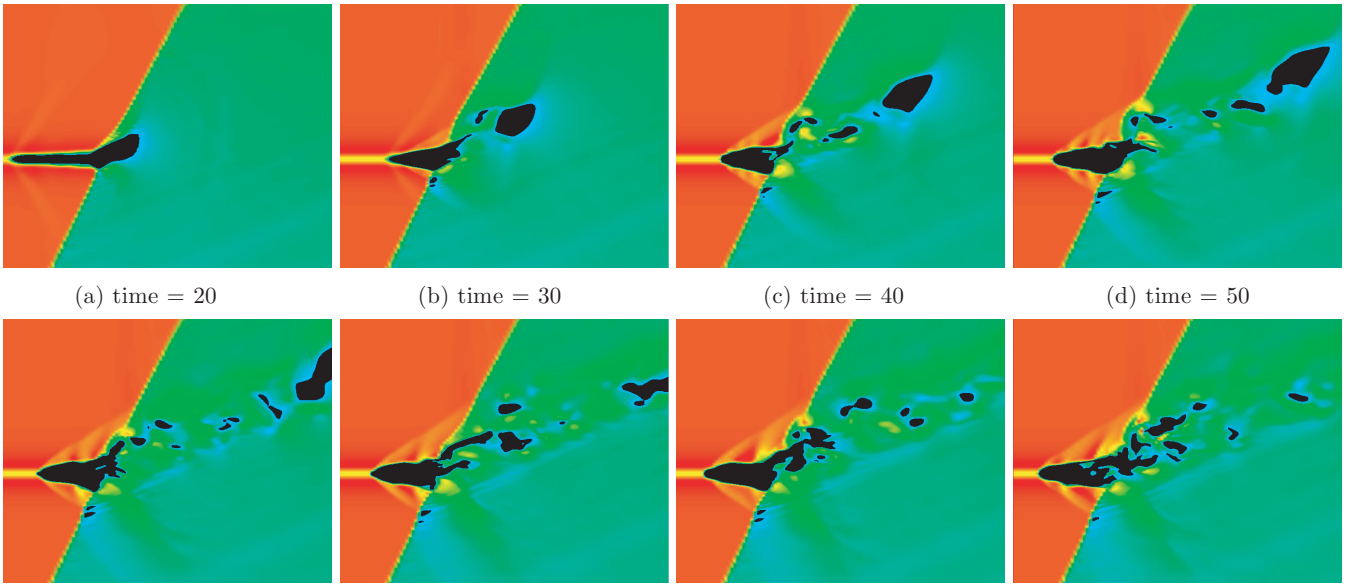

(a) time = 20 (b) time = 30 (c) time = 40 (d) time = 50

(e) time = 60 (f) time = 70 (g) time = 80 (h) time = 90

FIG. 14. (Color online) Temporal evolution of Mach number contours for $q = 0.6$, $\mu = 0.2$ at $M_\infty = 2.0$ (black areas show subsonic regions).

C. Breakdown evaluation from the static pressure and helicity density

The extent of breakdown on the streamwise vortex is most appropriately evaluated by the helicity density, for the following reason. If the axis of a streamwise vortex is aligned with the velocity vector of the main stream, the helicity is large, but if the velocity deficit is large or reversed flow is present, the helicity reduces or reverses its sign. Therefore, the helicity can elucidate whether streamwise vortices are collapsed by shock waves under certain conditions.

The temporal evolutions of the helicity density contours are plotted in Figs. 17 and 18, for $q = 0.2$ and 0.6, $\mu = 0.2$, respectively, at $M_\infty = 2.0$. At low circulation ($q = 0.2$), the streamwise vortex is stable and almost steady following interaction with the oblique shock. However, when the circulation increases to $q = 0.6$, the streamwise vortex breaks into small-scale structures. In contrast to $q = 0.2$, the interaction induces a dimple in the vortex for $q = 0.6$, which appears at an early stage. Unsteady vortical structures, such as sphere wakes, are released from the interference region to downstream. This result suggests that the phenomenon manifests from the absolute instability.

Second, the static pressures and the helicities (normalized by inflow conditions on the vortex center) are plotted in Fig. 19. The bottom panels of this figure are viewed from the axis of

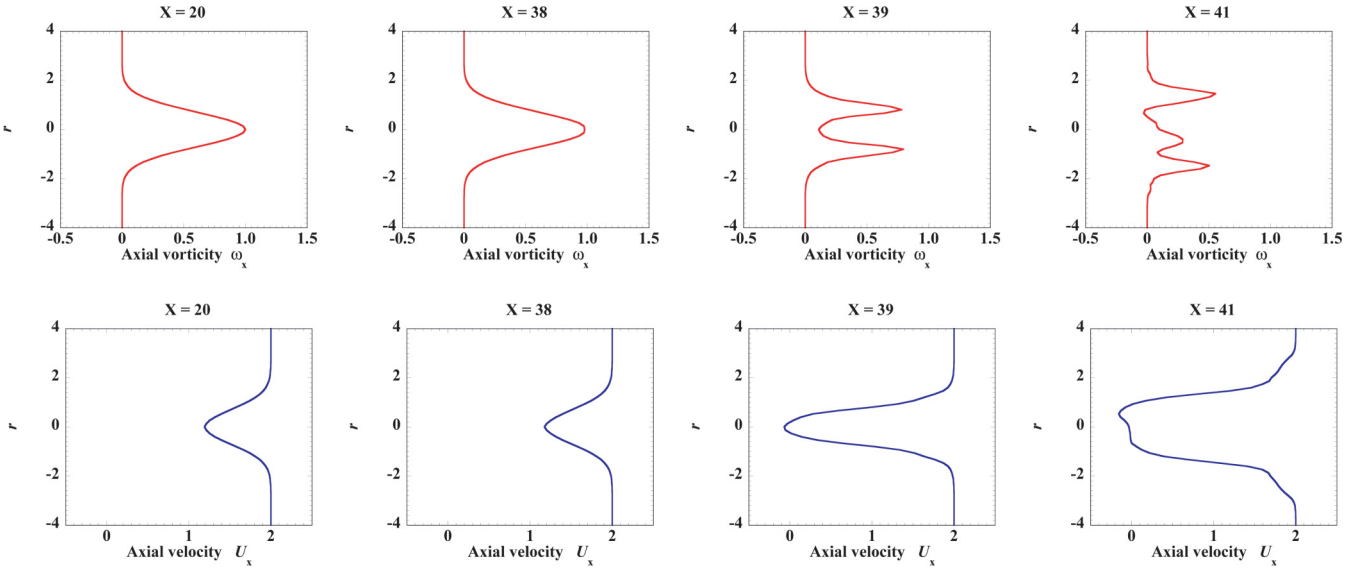

FIG. 15. (Color online) (Top) normalized axial vorticity profiles and (bottom) axial velocity profiles (normalized by local sonic speed), in the vicinity of an interaction between a streamwise vortex $q = 0.4$, $\mu = 0.4$ and an oblique shock wave intercepting at $\beta = 65°$, $M_\infty = 2.0$.

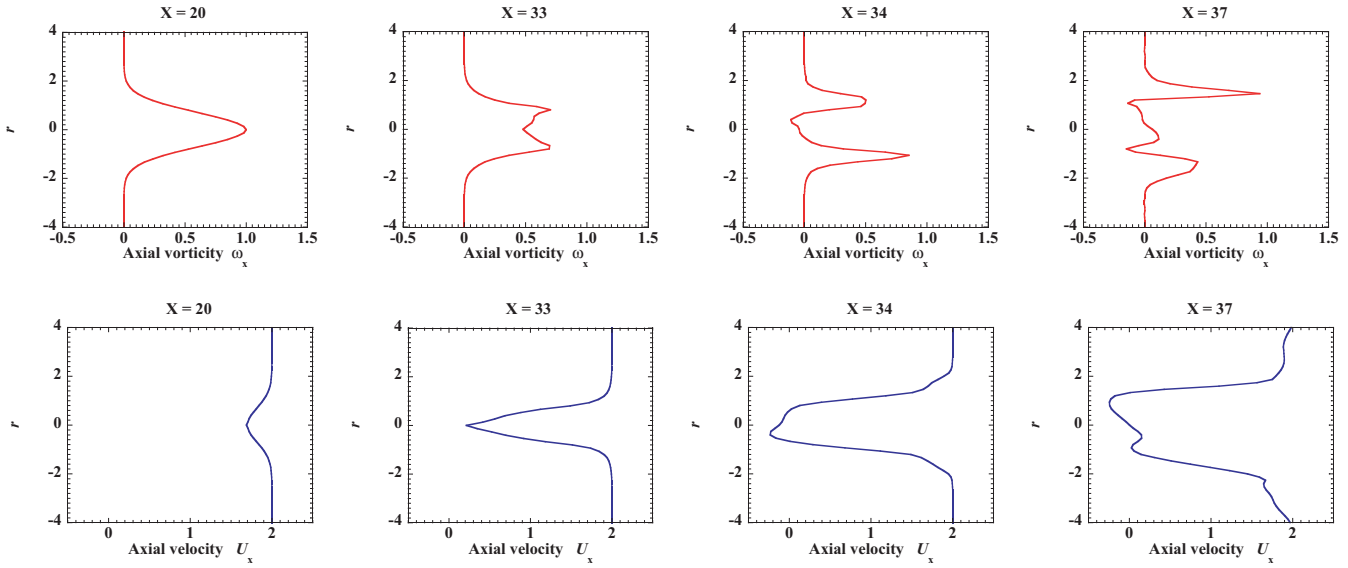

FIG. 16. (Color online) (Top) normalized axial vorticity profiles and (bottom) axial velocity profiles (normalized by the local sonic speed), in the vicinity of an interaction between a streamwise vortex $q = 0.6$, $\mu = 0.2$ and an oblique shock wave intercepting at $\beta = 65^\circ$, $M_\infty = 2.0$.

the vortex center along the turning angle behind the shock, for various upstream vortices at $M_\infty = 2.0$ (each distribution is time averaged). In all of the static pressure distributions, the pressure rises in one or two steps and recovers downstream. The numerical results indicate that if the flow field cannot be adapted to the shock by a one-step pressure rise, the field advances a weakened convex shock front and creates a hill in the pressure distribution. As a result, although the flow can get over the large pressure gradient from the hill, the streamwise vortex breakdown occurs. The results of Fig. 19 can be summarized as follows: if *no breakdown* occurs, (I) a single pressure rise is induced by the oblique shock; (II) provided that the shock front is not convex, the helicity is maintained from upstream to where the shock wave intercepts the vortex; (III) the helicity is positive, i.e., a large-scale vortex structure persists behind the interference. In the case of *breakdowns*, (IV) multiple pressure rises occur; (V) the helicity disappears behind the shock; (VI) the position of the shock wave and vortex interaction is shifted forward. On the basis of these rules, numerical results are plotted in Fig. 20. Unfortunately, in contrast to the previous analysis of NSVI, breakdown occurs inside the critical curve derived from Eq. (13). The next subsection discusses ways of correcting this discrepancy.

D. The effects of circulation and Mach number on breakdown

As mentioned above, vortex breakdown occurs within the critical curve of onset in Fig. 5. However, the relationship

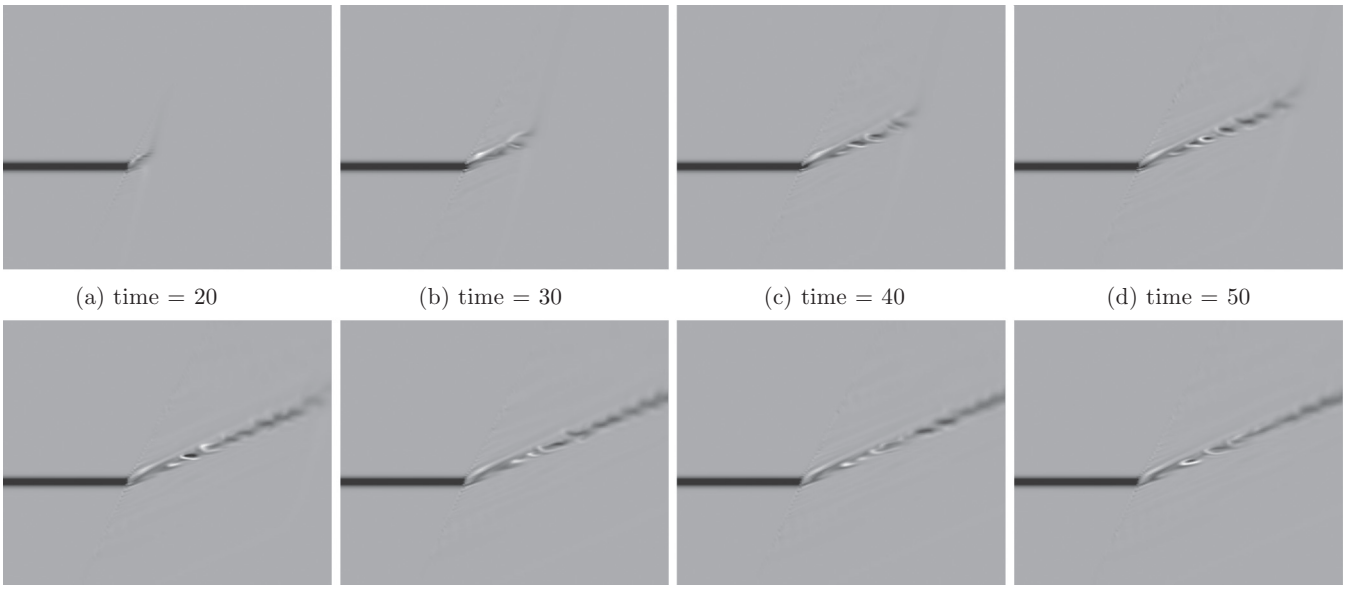

(a) time = 20 (b) time = 30 (c) time = 40 (d) time = 50

(e) time = 60 (f) time = 70 (g) time = 80 (h) time = 90

FIG. 17. Temporal evolution of the helicity density contours. Parameters: $q = 0.2$, $\mu = 0.2$, $M_\infty = 2.0$.

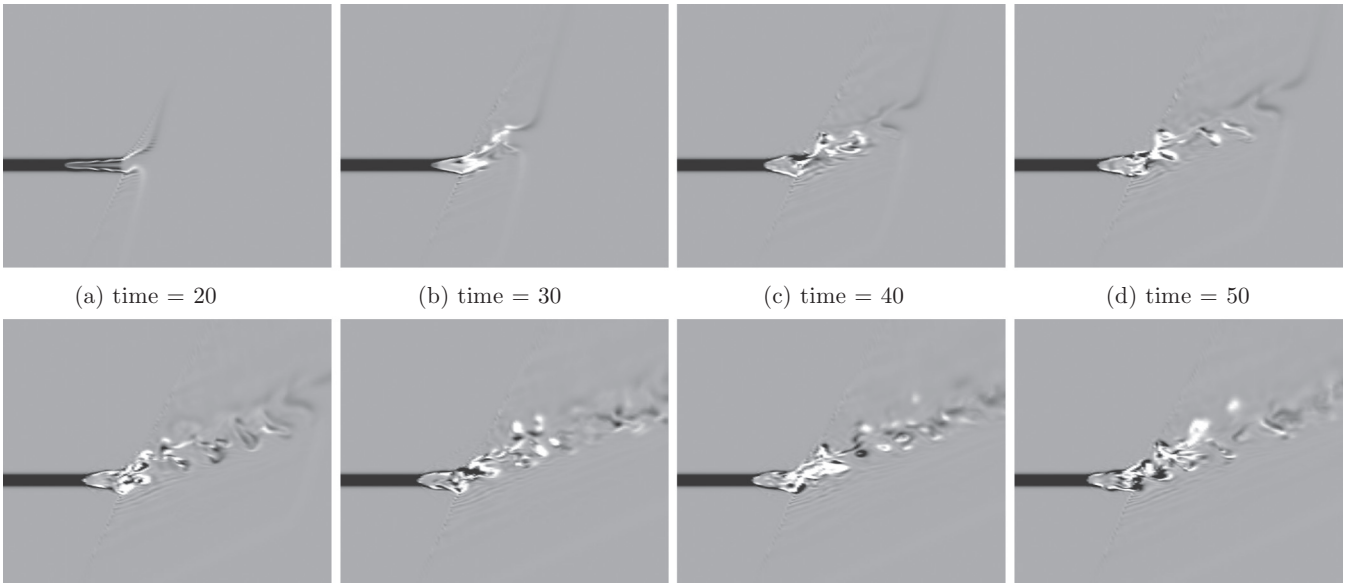

(a) time = 20 (b) time = 30 (c) time = 40 (d) time = 50

(e) time = 60 (f) time = 70 (g) time = 80 (h) time = 90

FIG. 18. Temporal evolution of the helicity density contours. Parameters: $q = 0.6$, $\mu = 0.2$, $M_\infty = 2.0$.

between the circulation and Mach number reveals an additional breakdown condition, which is not required in NSVI at $M_\infty = 2.0$. The interactions are always accompanied by perturbations. Under supersonic conditions, large perturbations give birth to shocklets. When a relative velocity component to perturbation locally exceeds the sonic speed, shocklets occur [35] and probably contribute to breakdown. According to this analysis, the shock wave and vortex interaction should induce breakdown if the azimuthal Mach number exceeds unity ($M_\theta \simeq qM_\infty > 1$). Physically this implies the burst of a supersonic swirl in the azimuthal direction. The inequality condition is given as

$$q > \frac{1}{M_\infty}. \tag{26}$$

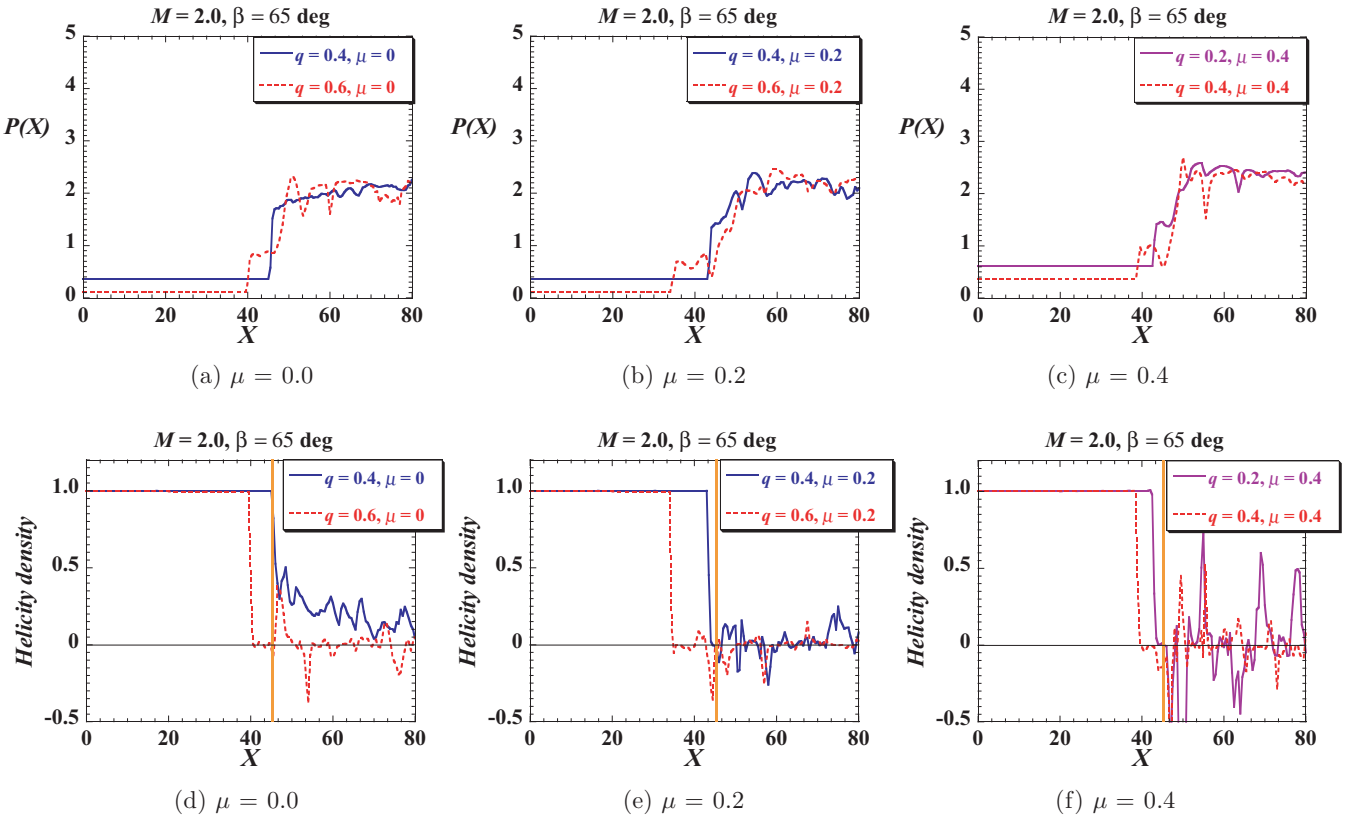

(a) $\mu = 0.0$ (b) $\mu = 0.2$ (c) $\mu = 0.4$

(d) $\mu = 0.0$ (e) $\mu = 0.2$ (f) $\mu = 0.4$

FIG. 19. (Color online) (Top) static pressures and (bottom) normalized helicity densities of streamwise variations along the lines of changing vortex center. Shock angle $\beta = 65^\circ$ at $M_\infty = 2.0$. The yellow dotted lines indicate where the vortex center crosses with the shock wave.

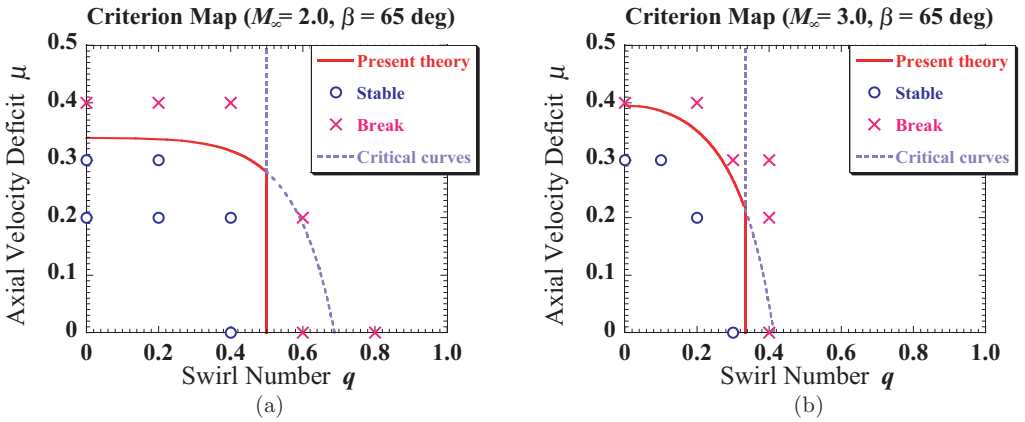

FIG. 20. (Color online) Comparison of theoretical critical curves and numerical results of vortex breakdown phenomena. Vortices are intercepted by a shock wave at $\beta = 65°$: (a) $M_\infty = 2.0$ and (b) $M_\infty = 3.0$. Stable or no effect (◯); vortex breakage (×); present theory (solid line).

Equation (26) implies that streamwise vortex structures are affected by shock waves in the stable region defined by Eq. (13). The onset of breakdown predicted from Eq. (13) and supplemented by Eq. (26) is mapped in Fig. 20. This prediction of the combined criteria now closely match the numerical results under various conditions of upstream vortices. Criterion (26) also explains why streamwise vortex breakdown occurs in OSVI at a small turning angle at $M_\infty = 5.0$, as reported in the literature [17,19]. Breakdown arises from the high Mach number. Thus, it is noteworthy that the shock-induced breakdown conditions for streamwise vortices are derived from simple equalities. In addition, the interaction field is probably suitable for generating the small-scale structures essential to mixing. Even if a streamwise vortex has recovered its velocity deficit and stabilized without a low-speed region in the freestream, vortices with large circulation or high Mach number can be disrupted by interacting with shock waves. This special property derives from the shock wave and vortex interaction.

Considering the similarities between shock-induced and subsonic vortex breakdown, much research to date has focused on the formation of stagnation points and reversed flows in shock-induced vortex breakdown. However, to properly understand supersonic vortex breakdown, we must specify the fundamental conditions for the onset. In applications, categorizing the collapse configurations of streamwise vortices is more important.

VI. CONCLUSIONS

This study has proposed a theoretically derived criterion for predicting the onset of supersonic vortex breakdown during interaction between an oblique shock wave and a streamwise vortex. The criterion involves two inequalities: One derived from the net pressure difference across the shock and the kinetic energy following the shock, and the other specifying that the product of the circulation and the freestream Mach number (i.e., the azimuthal Mach number) be greater than unity. The theory was tested in numerical formulations of the three-dimensional Navier-Stokes equations, conducted at $M_\infty = 2.0$ and 3.0. The vortex breakdowns of numerical simulations were reasonably determined by the time-average fields, provided that multiple pressure increases occurred, and the helicity disappeared behind the oblique shock wave, along the line of the vortex center. Moreover, it was confirmed that the Mach number distributions in a convex OSVI interaction region become subsonic, consistent with experiments [10]. Meanwhile, the axial vorticity profiles in the interaction region were highly unstable, and established a hollow distribution [34]. Since a number of spiral vortical structures are readily formed from such a vorticity profile, breakdown formation may be related to the changing local profiles. In any case, the local mean profiles are closely associated with the instability property. It is also necessary to consider kinds of breakdown in terms of this property.

The author has investigated mixing enhancement by subjecting isolated supersonic streamwise vortices to small disturbances, and noting their vortex instability [23]. Without shock wave and vortex interactions, streamwise vortices become rotationally stable with increasing circulation q. Instability also decreased with increasing freestream Mach number M_∞, due to compressibility effects. In contrast, the results of the present study are intriguing because breakdown onset was enhanced at higher circulation, and vortices could be disrupted by the interaction even at small oblique shock angles and high Mach number. Furthermore, a temperature rise behind the shock would confer major advantage to supersonic combustion. From the proposed theory, we can identify favorable mixing and combustion conditions over a wide range of Mach number, using vortex breakdown induced by shock wave and vortex interactions.

ACKNOWLEDGMENTS

The author thanks Emeritus Professor M. Nishioka for his support and encouragement. This work was partly supported by a Grant-in-Aid for Scientific Research (No. 20560739, No. 21226020) from the Ministry of Education, Culture, Sports, Science and Technology, Japan.

[1] O. Lucca-Negro and T. O'Doherty, Prog. Energy Combust. Sci. **27**, 431 (2001).
[2] S. Leibovich, AIAA J. **22**, 1192 (1984).
[3] J. M. Delery, E. Horowitz, O. Leuchter, and J. L. Solignac, Rech. Aerosp. **2**, 1 (1984).
[4] J. M. Delery, Prog. Aerosp. Sci. **30**, 1 (1994).
[5] I. M. Kalkhoran and M. K. Smart, Prog. Aerosp. Sci. **36**, 63 (2000).
[6] V. V. Zatoloka, A. K. Ivanyushkin, and A. V. Nikolayev, Fluid Mech. Sov. Res. **7**, 153 (1978).
[7] F. E. Marble, E. E. Zukoski, J. W. Jacobs, G. J. Hendricks, and I. A. Waitz, AIAA Paper 90–1981 (1990).
[8] O. Metwally, G. S. Settles, and C. C. Horstman, AIAA Paper 89–0082 (1989).
[9] L. N. Cattafesta and G. S. Settles, AIAA Paper 92–0315 (1992).
[10] M. K. Smart, I. M. Kalkhoran, and S. Popovic, Shock Waves **8**, 243 (1998).
[11] O. A. Kandil, H. A. Kandil, and C. H. Liu, in *Proceedings of the IUTAM Symposium on Fluid Dynamics of High Angle of Attack*, edited by R. Kawamura and Y. Aihara (Springer, Berlin, 1993), p. 192.
[12] K. R. Meadows, A. Kumar, and M. Y. Hussaini, AIAA J. **29**, 174 (1991).
[13] G. Erlebacher, M. Y. Hussaini, and C.-W. Shu, J. Fluid Mech. **337**, 129 (1997).
[14] M. Klaas, W. Schröder, and W. Althaus, AIAA Paper 2005–4652 (2005).
[15] G. Corpening and J. D. Anderson, AIAA Paper 89–0674 (1989).
[16] D. P. Rizzetta, AIAA J. **35**, 209 (1997).
[17] A. Nedungadi and M. J. Lewis, AIAA J. **34**, 2545 (1996).
[18] O. Thomer, W. Schröder, and E. Krause, Proceedings of the International Conference RDAMM–2001, Vol. 6 (2001), p. 737.
[19] A. A. Zheltovodov, E. A. Pimonov, and D. D. Knight, Shock Waves **17**, 273 (2007).
[20] L. N. Cattafesta III, Ph.D. thesis, Pennsylvania State University, 1992.
[21] K. Mahesh, Phys. Fluids **8**, 3338 (1996).
[22] M. K. Smart and I. M. Kalkhoran, AIAA J. **35**, 1589 (1997).
[23] T. Hiejima, Phys. Fluids **25**, 114103 (2013).
[24] S. Ragab and M. Sreedhar, Phys. Fluids **7**, 549 (1995).
[25] Y. Wada and M.-S. Liou, AIAA Paper 94–0083 (1994).
[26] P. L. Roe, J. Comput. Phys. **43**, 357 (1981).
[27] X. Deng and H. Zhang, J. Comput. Phys. **165**, 22 (2000).
[28] A. Jameson, W. Schmidt, and E. Turkel, AIAA paper 81–1259 (1981).
[29] T. J. Poinsot and S. K. Lele, J. Comput. Phys. **101**, 104 (1992).
[30] V. N. Zudov, A. Shevchenko, and P. K. Tretyakov, in *20th International Congress on Instrumentation in Aerospace Simulation Facilities* (IEEE, Washington, DC, 2003), p. 258.
[31] N. W. Battam, D. G. Gorounov, G. L. Korolev, and A. I. Ruban, J. Fluid Mech. **504**, 301 (2004).
[32] I. M. Kalkhoran, M. K. Smart, and F. Y. Wang, J. Fluid Mech. **369**, 351 (1998).
[33] J. Jeong and F. Hussain, J. Fluid Mech. **285**, 69 (1995).
[34] A. Michalke and A. Timme, J. Fluid. Mech. **29**, 647 (1967).
[35] W. M. Chan, K. Shariff, and T. H. Pulliam, J. Fluid Mech. **253**, 173 (1993).